Nano Research

Open Access

Research Article

Constructing low-reflection Ni@C/CNT/PIA//CF composite fiber membrane with "absorption–reflection–reabsorption" tuned EMI shielding performance

Shuaimin Zheng[1], Songqi Liu[1], Taghrid S. Alomar[2], Hu Liu[1], Weihua Chen[3], Najla AlMasoud[2], Duo Pan[1] ✉, Renbo Wei[4], Hassan Algadi[5], Chuntai Liu[1], Zhanhu Guo[6], and Changyu Shen[1]

[1] *Key Laboratory of Materials Processing and Mold (Zhengzhou University), Ministry of Education; National Engineering Research Center for Advanced Polymer Processing Technology, Zhengzhou University, Zhengzhou 450001, China*
[2] *Department of Chemistry, College of Science, Princess Nourah bint Abdulrahman University, P.O. Box 84428, Riyadh 11671, Saudi Arabia*
[3] *College of Chemistry, Zhengzhou University, Zhengzhou 450001 China*
[4] *Institute of Low-Carbon Technology Application, School of Chemical Engineering, Northwest University, Xi'an 710069, China*
[5] *Department of Electrical Engineering, Faculty of Engineering, Najran University, Najran 11001, Saudi Arabia*
[6] *Advanced Materials Division, Engineered Multifunctional Composites (EMC) Nanotech LLC, Knoxville, TN 37934, USA*

Cite this article: *Nano Research*, **2026**, *19*, 94908888. https://doi.org/10.26599/NR.2026.94908888

ABSTRACT: Low-reflection electromagnetic interference (EMI) shielding materials can effectively avoid secondary pollution of electromagnetic waves through high absorption rates. However, a single structural design of EMI shielding materials is difficult to simultaneously achieve low reflectivity and high shielding efficiency. Here, a synthetic Ni@C/carbon nanotube (CNT)/polyimide (PI) porous aerogel is built and utilized as the electromagnetic wave absorption layer and a highly conductive carbon fiber (CF) fabric serves as the bottom reflective layer. Through a clever two-layer coupling design, the Ni@C/CNT/PIA//CF composite achieves the efficient shielding mechanism of "absorption–reflection–reabsorption". In the X-band, the electromagnetic wave absorption coefficient is 0.89, and the total shielding efficiency (SE_T) reaches 50.5 dB, the excellent EMI shielding performance is attributed to the coupling structure optimizing impedance matching, extending electromagnetic wave propagation paths, and enhancing multiple scattering and interface polarization. Moreover, based on the compressive elastic recovery property of the PI matrix, the dielectric property of Ni@C/CNT, the photothermal storage property of CF, combined with the special structure design and thermal stability of the overall composite, Ni@C/CNT/PIA//CF also exhibits ideal force-resistance sensing, photothermal conversion, and flame-retardant properties. This work offers a promising strategy for next-gen EMI shielding materials with balanced high absorption, low reflection, and integrated functions.

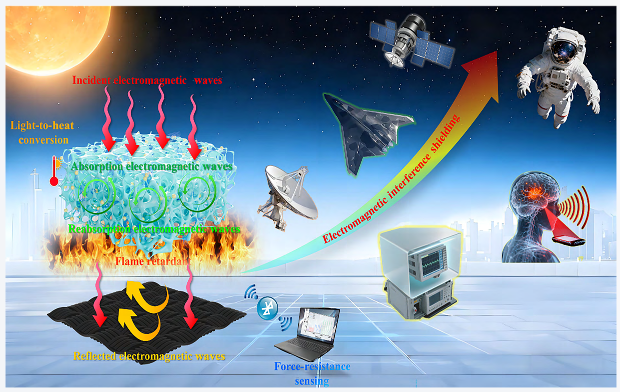

KEYWORDS: electromagnetic interference (EMI), shielding materials, two-layer coupling structure, absorption–reflection–reabsorption, low reflectivity, integrated functions

1 Introduction

With the rapid development of science and technologies such as 5G communication, intelligent wearable electronic devices, and aerospace, human society has entered an intelligent era highly dependent on electromagnetic signals [1, 2]. However, from daily civilian use to extreme deep space applications, external electromagnetic interference (EMI) not only leads to performance degradation of electronic devices and distortion of data transmission, but also poses security threats in key fields such as aerospace, biomedice [3–5]. Therefore, efficient shielding materials have become a research focus for resisting electromagnetic wave interference [6].

Received: April 12, 2026; **Revised:** May 23, 2026
Accepted: May 27, 2026

✉Address correspondence to panduonerc@zzu.edu.cn

Traditional conductive materials such as metal foils exhibit effective EMI shielding performance due to their high electrical conductivity and reflectivity [7]. However, their electromagnetic wave reflection coefficient typically exceeds 0.5, resulting in severe secondary electromagnetic pollution [8]. Moreover, their rigidity and high weight make them unsuitable for the flexibility requirements of modern electronic devices and the lightweight demands of extreme aerospace applications [9, 10]. Therefore, the ideal EMI shielding material needs to choose flexible fibers or lightweight aerogel materials to achieve a balance between high absorption and low reflection [11, 12]. On one hand, optimizing the interface impedance matching makes more electromagnetic waves enter the material interior [13, 14]. On the other hand, by designing the structure and adjusting the filler ratio to achieve multiple reflections and absorption of electromagnetic waves inside the material [15, 16]. Its goal is to achieve simultaneous high total shielding effectiveness with low surface reflection coefficient. However, this goal is hindered by an inherent technical challenge, which is the mutually restrictive between the excellent impedance matching for low reflection and strong electromagnetic dissipation for high shielding [17, 18].

Aerogels have emerged as ideal carriers for constructing high-efficiency EMI shielding due to their lightweight, three-dimensional (3D) porous structure, and tunable electromagnetic parameters [19, 20]. However, the insulation characteristics of common aerogels such as cellulose and polyimide, severely restrict their electromagnetic wave absorption ability, exhibiting an EMI shielding effectiveness of less than 1 dB even at millimeter thickness. In recent years, researchers have attempted to composite conductive and magnetic fillers into polymer aerogels to obtain low reflection and high absorption electromagnetic wave composites, but there are still some limitations [21–23]. For instance, Mai et al. [24] fabricated a zeolitic imidazolate frameworks (ZIF)-derived magnetic nanocage/MXene/nanocellulose bilayer aerogel for studying low-reflection EMI shielding performance, although the obtained aerogel achieved an EMI shielding effect of 35.1 dB (R = 0.28), the synergistic loss effect of the dielectric MXene and the ZIF-derived magnetic particles was not systematically explored by adjusting their proportion. Luo et al. [25] prepared carbon nanotubes (CNTs)@$CoFe_2O_4$/polyimide aerogel with anisotropic structure by a directional freezing process. By adjusting the addition ratio of CNTs and $CoFe_2O_4$, the optimum reflection loss of the composite aerogel can reach −54.4 dB. However, there are still a certain number of electromagnetic waves radiating into the environment transmit the sample. According to the current research status, there are three defects in the construction of low reflection EMI shielding based on aerogel materials: First, there is no thorough in-depth optimization of the proportion of conductive/magnetic fillers to achieve the triple balance of dielectric loss/magnetic loss/impedance matching by optimizing conductive/magnetic filler proportion [26]; Second, most research works mainly relies on a single attenuation mechanism of "reflection" or "absorption", lacking a closed-loop path to maximize the internal dissipation of incident electromagnetic waves [27]; Third, there is a lack of flexible integration and adaptability between EMI shielding performance and other multifunctional applications [28].

As illustrated in Fig. 1, in this work, a 3D porous polyimide aerogel (PIA) uniformly dispersed with CNT and magnetic Ni@C nanoparticles served as the main electromagnetic wave absorbing layer, while a highly conductive carbon fiber (CF) fabric acted as the backside reflection layer for residual transmitted waves. This two-layer coupling structure constructs a closed-loop "absorption–reflection–reabsorption" EMI shielding mechanism: the aerogel absorbs most incident waves with low surface reflection, and the CF fabric reflects all penetrating residual waves back for reabsorption. Thanks to this coupling structure, when the ratio of Ni@C to CNT is adjusted to 1:1, the Ni@C/CNT/PIA//CF (NCCPA/CF) composite achieves an EMI shielding effectiveness of 50.5 dB in the X-band and an absorption coefficient of 0.89. The excellent electromagnetic wave absorption performance endows it with potential applications in daily electronic communication and military radar stealth. Moreover, attributed to the excellent mechanical toughness of PIA, the synergistic effect of electromagnetic fillers, and the thermal stability of CF, NCCPA/CF exhibits multifunctional integration of pressure sensing, photothermal conversion, and flame retardancy. Therefore, this work holds significant guiding significance for electromagnetic wave protection in fields such as wearable electronic products and aerospace-military equipment.

2 Experimental methods

2.1 Materials

Nickel nitrate ($Ni(NO_3)_2·6H_2O$, AR) was purchased from Tianjin Kemiou Chemical Reagent Co., Ltd. Carboxylated multi-walled carbon nanotubes (MWCNT, purity ≥ 90%) were obtained from Suzhou Institute of Nano-Tech and Nano-Bionics (SINANO). Dopamine hydrochloride ($C_8H_{11}NO_2·HCl$, 98%) was provided by Hebei Chuancheng Metal Materials Co., Ltd. N,N-Dimethylacetamide (DMAc, ≥ 99.8%), 4,4′-diaminodiphenyl ether (ODA, 98%), 3,3′,4,4′-biphenyltetracarboxylic dianhydride (BPDA, 97%), triethylamine (TEA, 99%), and tris(hydroxymethyl) aminomethane (Tris) were purchased from Shanghai Aladdin Biochemical Technology Co., Ltd. Anhydrous ethanol (AR) was provided by Tianjin Fuyu Fine Chemicals Co., Ltd. Carbon fiber fabric was purchased from Yixing Huifeng Carbon Fiber Technology Co., Ltd. Deionized water (DI water, H_2O) was supplied in unlimited quantities by the laboratory.

2.2 Preparation of nickel-carbon (Ni@C) powder

First, nickel hydroxide ($Ni(OH)_2$) was prepared by a hydrothermal reaction using anhydrous ethanol, deionized water, $Ni(NO_3)_2·6H_2O$ and urea as raw materials. Then, nickel oxide (NiO) powder was obtained through high-temperature calcination. Subsequently, a mixture solution of Tris, deionized water, anhydrous ethanol, NiO powder and polydopamine hydrochloride ($C_8H_{11}NO_2·HCl$) was subjected high-temperature calcination and thermal reduction to obtain the nickel-carbon (Ni@C) powder. The detailed preparation process is provided in the Electronic Supplementary Material (ESM).

2.3 Preparation of NCCPA/CF

Ni@C and CNT were added to 20 mL deionized water in a predetermined ratio and treated with an ice water bath ultrasonic for 30 min to form a uniform mixed solution. The dispersion was transferred to a 250 mL three-necked flask, polyamic acid (PAA, the synthesis process is detailed in the ESM) and triethylamine were added sequentially and mechanically stirred at a speed of 300 rpm

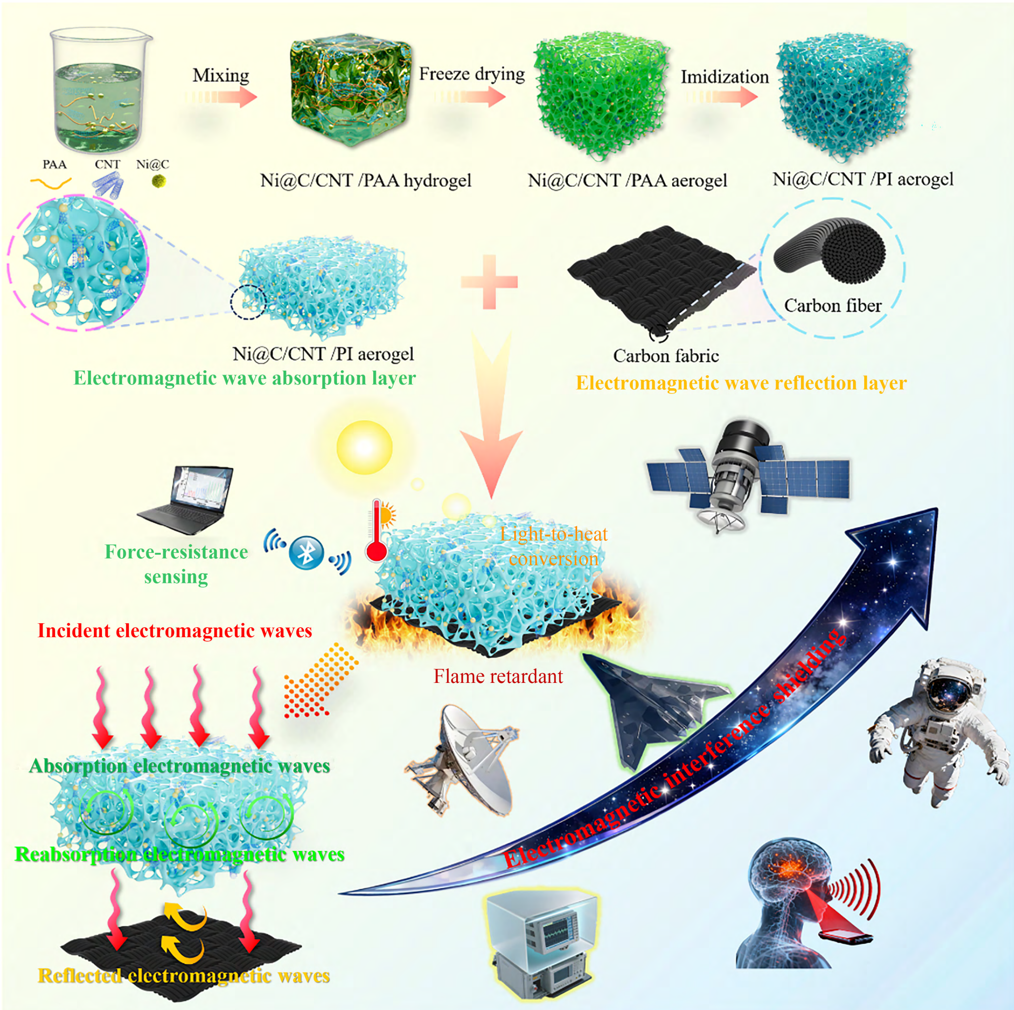

Figure 1 The preparation process and potential application concept diagram of the Ni@C/CNT/PIA//CF composite with a two-layer coupling structure.

for 2 h at room temperature to ensure sufficient cross-linkin. Next, the reaction solution was poured into a custom mold and quickly frozen in liquid nitrogen at −196 °C for 30 min to solidify the system and form the Ni@C/CNT/PAA hydrogel precursor. Then, the precursor was transferred to a freeze dryer and dried under vacuum at −48 °C and 15 Pa for 72 h to remove the solvent and retain the 3D porous structure, resulting in a lightweight Ni@C/CNT/PAA aerogel. Next, the obtained composite aerogel was placed in a tube furnace and thermally annealed at 300 °C for 2 h under argon atmosphere to complete the imidization process, ultimately obtaining a polyimide (PI) based aerogel Ni@C/CNT/PIA (simplified as NCCPA). NCCPA is named $NCC_{m\text{-}n}PA$ (*m-n* is 2-1, 1-1, and 1-2) according to the difference in the addition ratio of Ni@C and CNT. Polyvinyl alcohol (PVA) was used as the interfacial crosslinker to achieve organic bonding between NCCPA and CF. Specifically, a 10 wt.% PVA aqueous solution was uniformly coated on one side of the CF fabric. The NCCPA aerogel was immediately flatly attached to the coated surface, and the assembly was placed in a vacuum pressing device and pressed at room temperature under 0.08 MPa for 2 h, allowing PVA to fully penetrate into the surface pores of the aerogel and form hydrogen bond crosslinking with oxygen-containing functional groups on the CF surface. Subsequently, the sample was dried in an oven at 60 °C for 12 h to complete curing, ultimately obtaining the NCCPA/CF two-layer coupling composite with robust interfacial bonding. According to the simple test results in Fig. S2 in the ESM, NCCPA/CF can easily withstand a pulling force of 100 g weights without any delamination.

2.4 Characterization

The morphology and microstructure were observed using a field emission scanning electron microscope (FESEM thermoscientifc Apreo C, USA). The chemical structure of the samples was characterized by a Fourier transform infrared spectrometer (FTIR, Nicolet 6700, USA) and an X-ray photoelectron spectrometer (XPS, Thermo Fisher Scientific K-Alpha$^+$, USA). Thermogravimetric analysis (TGA) of PI and $NCC_{m\text{-}n}PA$ was performed in a nitrogen atmosphere using a thermogravimetric analyzer (TG209F3, Germany) at a heating rate of 10 °C/min. The spectral absorption in the ultraviolet (UV), visible (Vis), and near-infrared (NIR) wavelength ranges (0.25–2.5 μm) was measured using a UV–Vis–NIR spectrophotometer (PerkinElmer, Lambda 1050+, Britain). The temperature-time variation of the sample surface during the photothermal conversion process was recorded by an infrared thermal imager (E60, FLIR, USA). The pressure-sensing performances were assessed using an electrochemical workstation (RST5000F) in conjunction with a universal testing machine (UTM2203). The electromagnetic parameters of Ni@C/CNT in the

X-band (8.2–12.4 GHz) were measured via the coaxial method using circular test samples with an inner diameter of 3.04 mm and an outer diameter of 7 mm. In this work, when determining the optimal ratio of Ni@C:CNT, Ni@C/CNT with all proportional ratios were dispersed in paraffin at a mass fraction of 10 wt.%. The EMI shielding performance of NCCPA/CF in the X-band was determined via the waveguide method.

3 Results and discussion

3.1 Characterization analysis

Figures 2(a) and 2(b) respectively show the SEM images of NiO and Ni@C microspheres. From Figs. 2(a) and 2(a_1), the NiO obtained through uniform hydrothermal reaction exhibits a microspherical

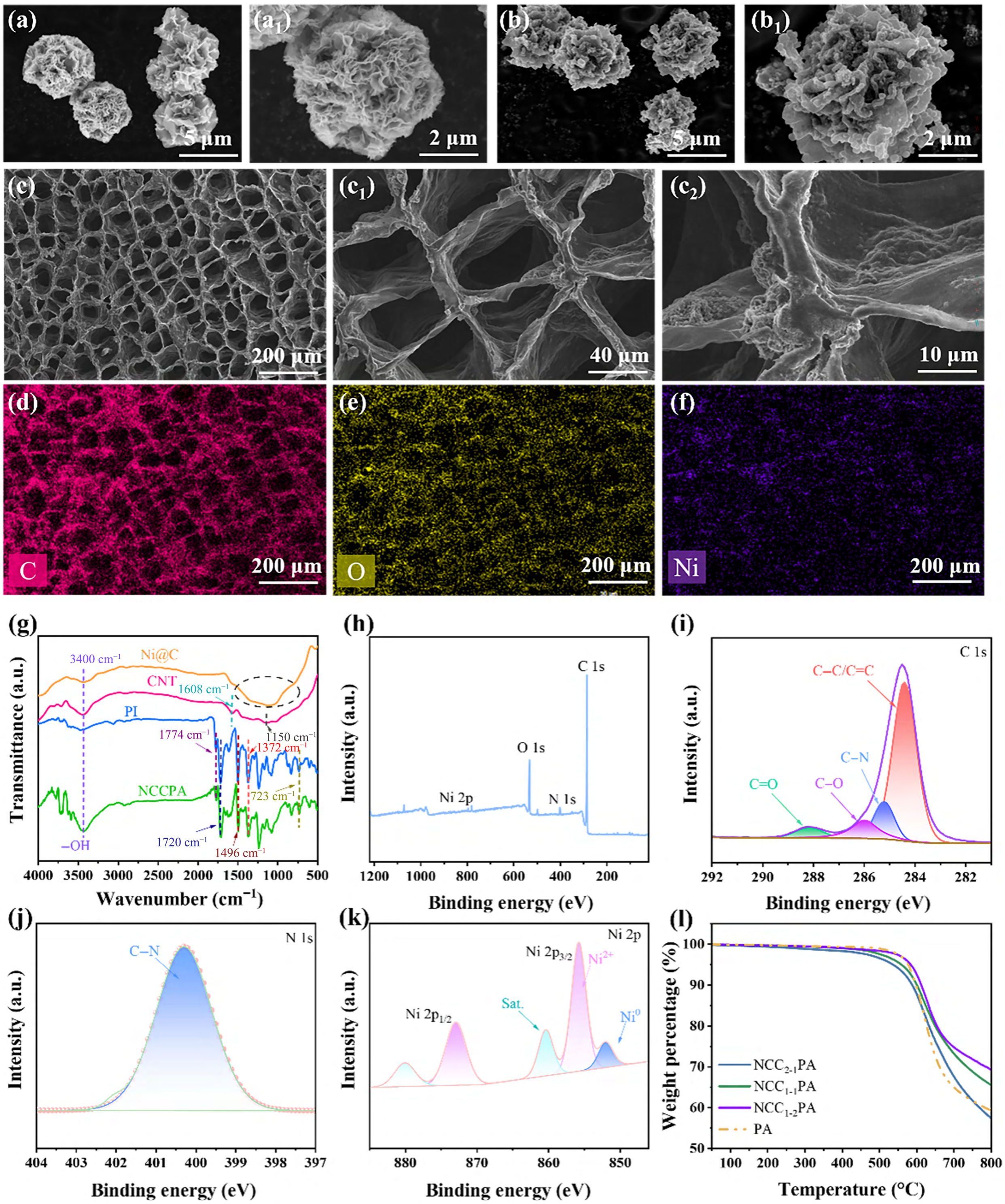

Figure 2 SEM images of ((a) and (a_1)) NiO, ((b) and (b_1)) Ni@C microspheres, and ((c)–(c_2)) the 3D porous network of the NCCPA. (d)–(f) Elemental mapping distributions of C, O, and Ni in the NCCPA. (g) FTIR spectra of PI, Ni@C, CNT, and $NCC_{1\text{-}1}PA$. (h) Full X-ray photoelectron spectrum of $NCC_{1\text{-}1}PA$. Fine X-ray photoelectron spectra of (i) C 1s, (g) N 1s, and (k) Ni 2p of $NCC_{1\text{-}1}PA$. (l) TGA curves of PI aerogel and NCCPA in nitrogen atmosphere.

morphology composed of nano-flower structures, with a microsphere diameter of around 5 μm. The nano-flower structure is conducive to the uniform coating of PDA modifiers [29]. Therefore, the Ni@C particles obtained through carbon thermal reduction still maintain the microspherical morphology of NiO, and more Ni–C heterojunction interfaces have been formed. From the morphology characterization in Fig. 2(c), it can be clearly seen that the obtained PI based aerogel composite presents a honeycomb like 3D cavity structure. The smooth honeycomb walls (Fig. 2(c_1)) indicate the uniform dispersion of the magnetic phase Ni@C and the conductive phase CNT. In addition, the high-resolution SEM images (Fig. 2(c_2)) also confirm that the Ni@C microspheres are uniformly embedded in the PI matrix. This conclusion is further validated by the uniform distribution of C, O, and Ni elements in the element mapping distribution diagram (Figs. 2(d)–2(f)).

From the FTIR spectra presented in Fig. 2(g), CNT shows two characteristic peaks at 1608 and 1150 cm^{-1}, corresponding to the stretching vibrations of the C=O bond and C–O bond in carboxyl groups, respectively [30, 31]. For Ni@C, a broad peak in the range of 800–1600 cm^{-1} originates from the combined contribution of high-temperature pyrolysis carbon structures (C–C and C=C bond) and the coordination interaction between Ni–C bond [32]. Furthermore, a distinct characteristic peak at 3400 cm^{-1} appears in the FTIR spectra of CNT and Ni@C, which corresponds to the stretching vibration of O–H in the surface hydroxyl groups [33]. This also provides a theoretical basis for the uniform dispersion of CNT and Ni@C in NCCPA. Two characteristic peaks appear at 1774 and 1720 cm^{-1} for both PI aerogel and NCCPA, which are attributed to the symmetric stretching vibration and asymmetric stretching vibration of the C=O bond in the imide ring, respectively [34, 35]. The characteristic peak observed at 1496 cm^{-1} originates from the stretching vibration of C=C in the benzene ring, while the peak at 1372 cm^{-1} is derived from the stretching vibration of the C–N bond. The peak at 723 cm^{-1} corresponds to the bending vibration of C=O in the imide ring. The appearance of the same characteristic peaks in PI aerogel and NCCPA provides strong evidence for the successful thermal imidization of PAA [36].

XPS was used to further analyze the chemical structure of NCCPA, in Fig. 2(h), the NCCPA shows an XPS peak of C 1s, O 1s, N 1s, and Ni 2p, which indicates that CNT, Ni@C, and PI have been successfully incorporated into the NCCPA. The high-resolution XPS of C 1s, N 1s, and Ni 2p for the NCCPA were analyzed in detail. Among them, the C 1s spectrum exhibits the following characteristic peaks: 284.8 eV corresponding to C=C/C–C, 285.6 eV corresponding to C–N, 286.3 eV corresponding to C–O, and 288.5 eV corresponding to C=O. The characteristic peak at 399.5 eV in the N 1s spectrum corresponds to the C–N [37]. These characteristic peaks collectively confirm the existence of the PI molecular structure (Figs. 2(i) and Figs. 2(j)). In addition, the characteristic peak at 852 eV indicates the presence of metallic Ni in the NCCPA (Fig. 2(k)). The presence of Ni^{2+} is discovered because during the synthesis of Ni@C, a thin oxide layer forms on the Ni surface, which can protect the core region of Ni from further oxidation. Trace amounts of Ni^{2+} are detected because the detection depth of XPS is only about 10 nm [38].

From the TGA characterization of PI and NCCPA (Fig. 2(l)), the slight weight loss before 550 °C indicates the completion of the desolvation and imidization process. This indicates that the PI aerogels possess excellent thermal stability, benefiting from the aromatic ring structure and the high bond energy of imide rings [39]. In addition, the residue content at 800 °C of $NCC_{1\text{-}2}PA$ is significantly higher than that of other samples, which may be due to the incorporation of more CNT with excellent thermal stability [40]. On the contrary, the residue content of $NCC_{2\text{-}1}PA$ composite aerogels is significantly lower than that of other samples, which may be attributed to the insufficient incorporation of CNT and the excessive Ni@C in this system, and these Ni@C particles exert a catalytic effect at high temperatures to accelerate the decomposition of the PI matrix [41].

3.2 Electromagnetic parameters and impedance matching of Ni@C/CNT

The dielectric loss and magnetic loss ability of composites are the key factors determining their electromagnetic wave absorption performance. The higher electrical conductivity of the material, the greater the probability of electromagnetic waves colliding with free electrons, which leads to more dielectric and polarization losses of the electromagnetic waves [42]. Magnetic loss achieves the attenuation of electromagnetic waves through the generation of heat or magnetic-induced eddy current resonance during the magnetization/demagnetization process of magnetic materials, thereby effectively reducing the penetration ability of electromagnetic waves and improving the absorption efficiency [43]. However, excessive conductive media can cause severe impedance mismatch between the surface of the composite and the air, resulting in strong interface reflection of incident electromagnetic waves and affecting the high absorption performance; While excessive magnetic media can reduce the polarization relaxation magnetic coupling ability of the composite, decrease magnetic loss, and deteriorate the electromagnetic wave attenuation performance [44]. Therefore, it is crucial to adjust the ratio of conductive/magnetic fillers to achieve a triple balance mode of “dielectric magnetic loss impedance matching” mainly based on electromagnetic wave absorption. The appropriate proportion can not only maximize the dielectric and magnetic loss capabilities, but also optimize the interface polarization of heterogeneous interfaces, achieving the goal of optimal absorption of electromagnetic waves.

Based on this, the appropriate addition ratio of Ni@C:CNT is of vital importance to the electromagnetic wave absorption performance of the composite. Figures 3(a)–3(c) show the real part (ε'), imaginary part (ε'') of complex permittivity, and dielectric loss tangent ($\tan\delta_\varepsilon$) under different Ni@C:CNT mass ratios. Compared with pure Ni@C (Fig. S3 in the ESM), the introduction of one-dimensional CNTs significantly enhanced the ε' and ε'' values of the Ni@C:CNT (2:1, 1:1, 1:2) composites. This is attributed to the weak conductivity of the zero-dimensional Ni@C microspheres, which fails to form a continuous conductive network. In addition, as the mass ratio of CNT increases, both ε' and ε'' show an upward trend, this is because the continuous 3D conductive network constructed by CNT enhances charge migration (electronic conduction loss), and the Maxwell–Wagner space charge polarization effect at the interface strengthens dielectric polarization loss [45]. Notably, the excessive aggregation of CNT in Ni@C:CNT (1:2) hinders polarization relaxation, resulting in a sharp drop of $\tan\delta_\varepsilon$ in the high-frequency region. For Ni@C:CNT (1:1), the values of ε', ε'', and $\tan\delta_\varepsilon$ throughout the entire frequency range are more stable compared to Ni@C:CNT (1:2), and are higher than that of Ni@C:CNT (2:1), indicating that the dielectric loss of the composite is more stable and durable at this content [46]. Figures 3(d)–3(f) presents the magnetic response characteristic parameter (real part

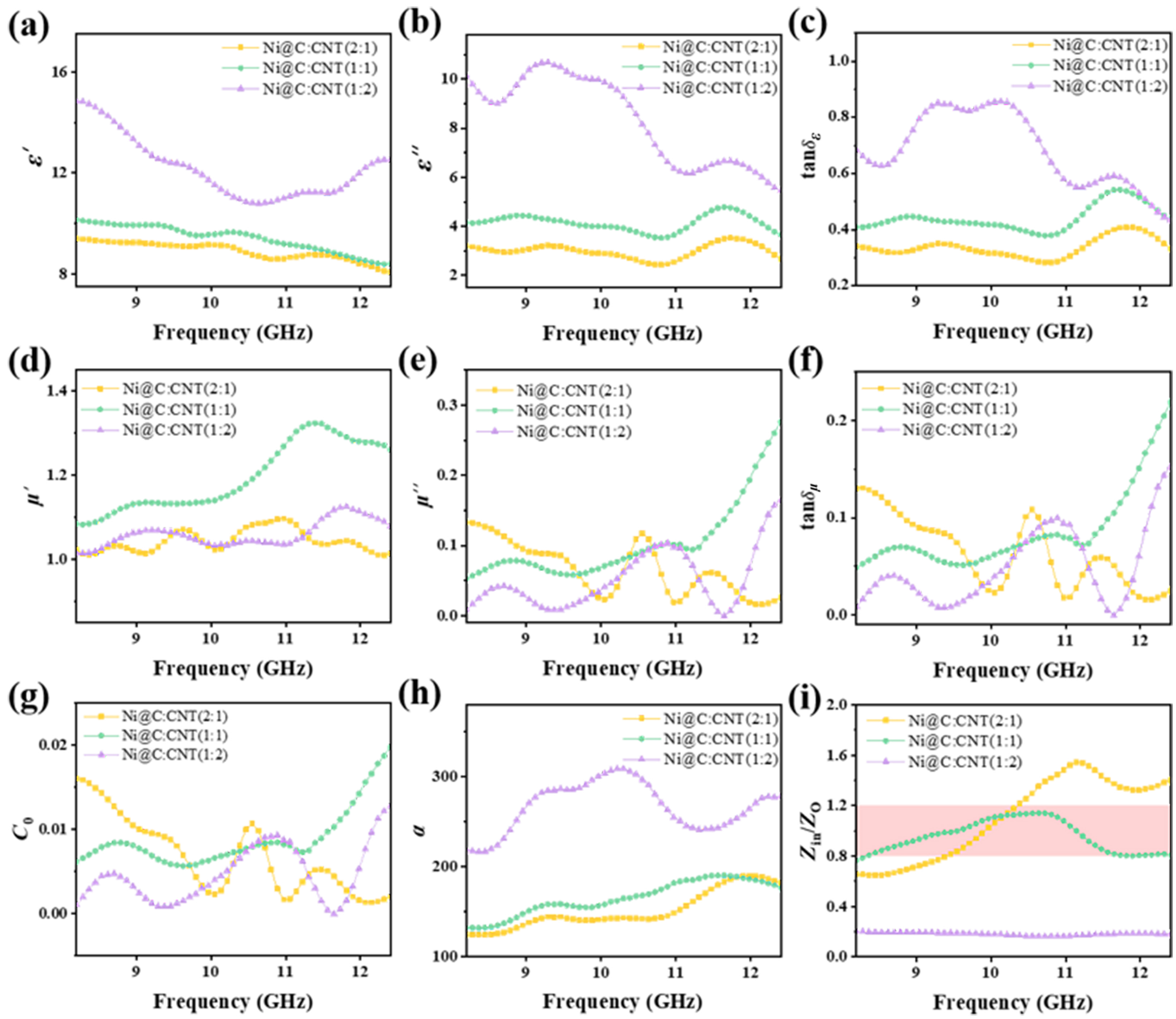

Figure 3 (a) Dielectric constant real part, (b) dielectric constant imaginary part, (c) dielectric loss angle $\tan\delta_\varepsilon$, (d) complex permeability real part, (e) complex permeability imaginary part, (f) magnetic loss angle $\tan\delta_\mu$, (g) eddy-current loss, (h) attenuation coefficient, and (i) perfect impedance matching of Ni@C:CNT.

μ', imaginary part μ'', and magnetic loss tangent $\tan\delta_\mu$) curves of Ni@C/CNT hybrid fillers. When the mass ratio of Ni@C to CNT is 1:1, the μ' value of Ni@C:CNT (1:1) is significantly higher than that of Ni@C:CNT (2:1) and Ni@C:CNT (1:2) throughout the X-band, indicating its excellent magnetic energy storage capacity (Fig. 3(d)). Moreover, the μ'' value of Ni@C:CNT(1:1) shows a steadily increasing trend (Fig. 3(e)), and the $\tan\delta_\mu$ is significantly higher than the other two samples in the high-frequency region (Fig. 3(f)), this is mainly attributed to the synergistic effect between the magnetic loss in Ni@C and the magnetic coupling effect caused by CNT. whereas for Ni@C:CNT(2:1), excessive Ni@C causes particle agglomeration, which hinders magnetic domain rotation and affects magnetic loss performance. The eddy current loss (C_0)–frequency (C_0–f) curves calculated via Eq. (S1) in the ESM are shown in Fig. 3(g). Similar to the test results of μ'' and $\tan\delta_\mu$, the C_0 value of Ni@C:CNT (1:1) shows an upward trend and is higher than Ni@C:CNT (2:1) and Ni@C:CNT (1:2) in the high-frequency region, this phenomenon is mainly attributed to the enhanced natural resonance of the nickel cores in Ni@C powder.

In general, a relatively high attenuation constant (α) and excellent impedance matching coefficient ($|Z_{in}/Z_0|$) are prerequisites for achieving superior electromagnetic wave absorption performance [47]. The α–f curves calculated via Eq. (S2) in the ESM are presented in Fig. 3(h), the α value of Ni@C:CNT (2:1) is relatively low, which is due to the low content of CNT, resulting in a smaller dielectric loss. For Ni@C:CNT (1:2), although it has a relatively high α value, the impedance mismatch limits its electromagnetic wave absorption performance [48]. Impedance matching coefficient ($Z = |Z_{in}/Z_0|$) is used to evaluate the degree of impedance matching between the material and free space. When the Z value is close to 1, it indicates that the electromagnetic waves in the air can easily enter the sample and achieve the purpose of absorption [49]. Combining Eq. (S3) in the ESM and the test results from Fig. 3(i), it can be seen that within the frequency range of 8.2–12.4 GHz, the $|Z_{in}/Z_0|$ curve of Ni@C:CNT (1:2) deviates significantly from the ideal value. In contrast, the $|Z_{in}/Z_0|$ curve of Ni@C:CNT (1:1) remains within the ideal impedance matching range across the entire X-band. Therefore, Ni@C:CNT (1:1) achieves an appropriate balance between the attenuation constant and impedance matching.

Appropriate impedance matching is the prerequisite for materials to mainly generate absorption losses in electromagnetic waves. Therefore, it is of great significance to further explore the close relationship between the absorption capacity of electromagnetic waves and impedance matching [50]. Figures 4(a)–4(c) show the corresponding $|Z_{in}/Z_0|$ values for three Ni@C:CNT mass ratios at different thicknesses. It can be clearly observed that for Ni@C:CNT(1:1), it has Z value closer to 1 (0.8–1.0) in the thickness range of 2 mm, and it achieves the best impedance matching around 10 GHz, indicating that at this ratio, the sample can achieve a low reflection and high absorption effect on electromagnetic waves. In contrast, although Ni@C:CNT (2:1) and Ni@C:CNT (1:2) respectively possess strong magnetic loss and electrical loss capabilities, impedance mismatch limits their electromagnetic wave absorption loss capacity. Radar cross section (RCS) simulations of Ni@C:CNT were performed using CST software to characterize the actual far-field absorption loss capability of the material [51]. The scattered signals in the figure are represented as blue bars, representing the signal strength of the electromagnetic wave emitted by the field source after it passes through the material. When the area of the plot is smaller and the color is bluer, the signal is weaker and the material's absorption loss capability is stronger. From Figs. 4(a_1)–4(c_1), compared with Ni@C:CNT(2:1) and Ni@C:CNT(1:2), Ni@C:CNT(1:1) exhibits the weakest scattering signals, which indicates that it has the best absorption loss capability in the X-band. The RCS values of Ni@C:CNT are shown in Figs. 4(a_2)–4(c_2), within the an-gular range of −90° to 90°, the RCS value of Ni@C:CNT(1:1) is the lowest and all values falling below −20 dB·m². The modulation of the electromagnetic wave loss mechanism by single fillers and different

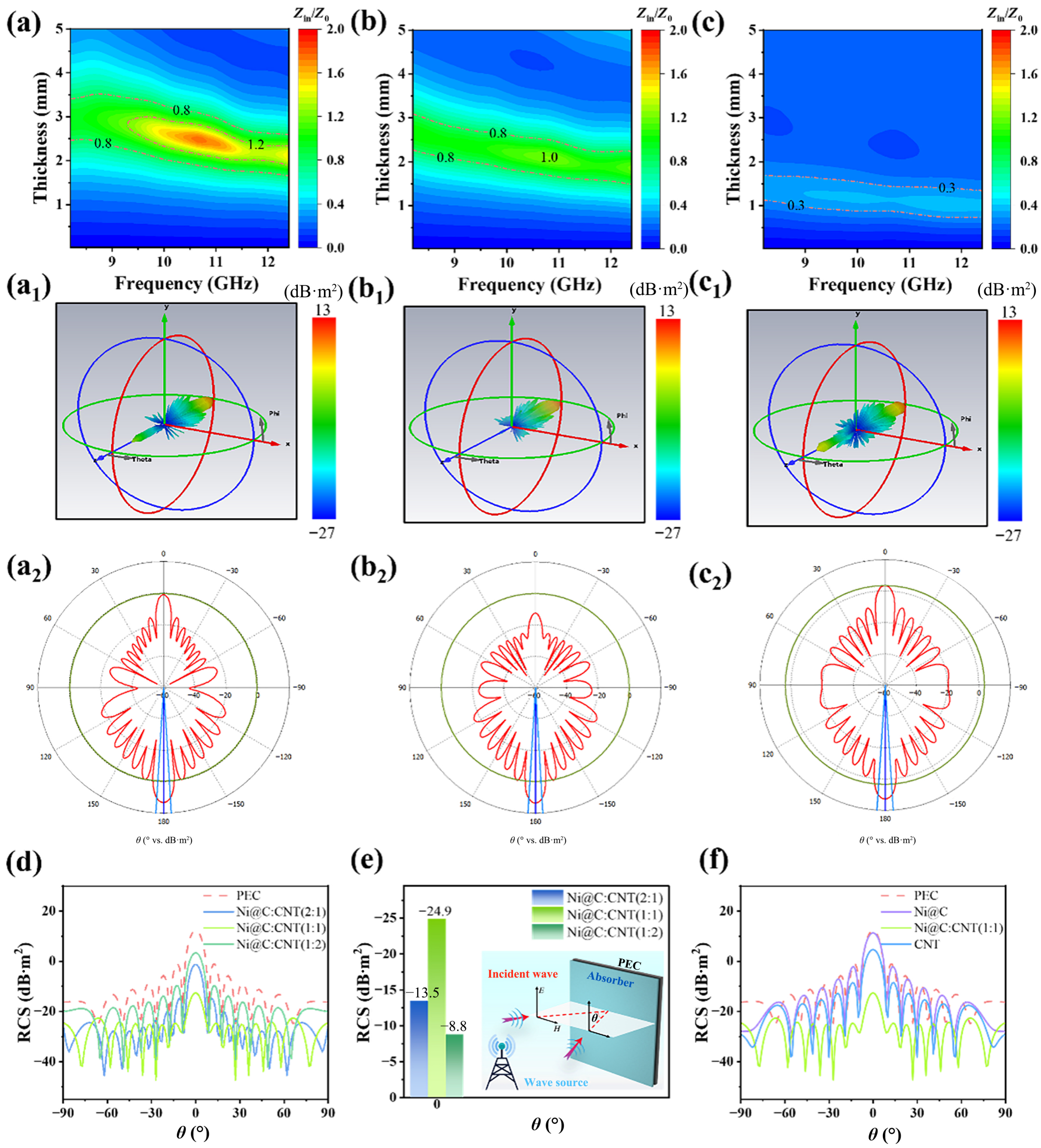

Figure 4 (a)–(c) 2D color-mapping of $|Z_{in}/Z_0|$, (a_1)–(c_1) 3D RCS plots of the PEC plane overlaid with Ni@C/CNT, and (a_2)–(c_2) RCS values within the angle range (−180° < θ < 180°) of Ni@C:CNT(2:1, 1:1, and 1:2). (d)–(f) Simulated RCS curves and RCS reduction values of the PEC plane and different samples.

hybrid components is further demonstrated by the simulated RCS values obtained from the two-dimensional (2D) curves in the Y–O–Z plane (Figs. 4(d)–4(f)), where the RCS values of Ni@C:CNT(1:1) are lower than those of Ni@C, CNT, Ni@C:CNT(2:1) and Ni@C:CNT(1:2). In addition, the theoretical RCS value obtained by subtracting the perfect electric conductor (PEC) plate (Fig. 4(e)) further demonstrates that Ni@C:CNT(1:1) could achieve ideal electromagnetic wave absorption capability.

3.3 Electromagnetic interference shielding performance of NCCPA/CF

In order to verify that the PI-based composite still maintains the absorption dominated EMI shielding performance under the optimal filler ratio, impedance matching and RCS simulation analyses were also conducted on $NCC_{1\text{-}1}PA$. From Fig. 5(a), $NCC_{1\text{-}1}PA$ with the optimal ratio shows that $|Z_{in}/Z_0|$ approaches 1 within a thickness range of 2–4 mm, indicating good impedance matching. By comparing the input impedance Z_{in} within this thickness range, it is found that the $NCC_{1\text{-}1}PA$ has the closest impedance matching to the ideal area when the overall thickness is 3 mm. The far-field electromagnetic wave absorption performance of $NCC_{1\text{-}1}PA$ was evaluated via RCS simulation (Fig. 5(b)) [52]. By analyzing the 2D RCS values through the Y–O–Z plane of the penetrated sample, it was found that the sample remained below −20 dB·m^2 within the range of −90° to 90°, indicating an effective electromagnetic wave absorption performance (Fig. 5(c)).

The waveguide method can accurately reflect the EMI protection efficacy and actual coefficients of NCCPA and NCCPA/CF. As shown in Fig. 5(d), it can be seen that the different PI-based NCCPA composites have little difference in shielding parameters (SE_T, SE_R, and SE_A, Table S1 in the ESM) due to their high porosity. Further conversion to shielding coefficient reveals that NCCPA mainly adopts the EMI shielding mechanism of absorption, and $NCC_{1\text{-}1}PA$ has the highest absorption coefficient (Fig. 5(e)), which verifies that when the Ni@C:CNT mass content is 1:1, a triple balance of “dielectric loss–magnetic loss–impedance matching” has been achieved in the composite, thereby minimizing the electromagnetic wave reflectivity and improving its absorption rate.

In order to maintain the absorption dominated EMI shielding mechanism of NCCPA and enhance the overall shielding performance, a CF reflective layer was ingeniously introduced at the lower layer of NCCPA. The resulting NCCPA/CF composite system with a two-layer coupling structure significantly improved the EMI shielding performance to around 50 dB (Figs. 5(f) and 5(g)), outperforming the single-layer NCCPA and CF. It is worth noting that based on the “absorption–reflection–reabsorption” mechanism, the absorption shielding coefficient of $NCC_{1\text{-}1}PA/CF$ was further enhanced to 0.89 (Fig. 5(h)). Figure 5(i) presents the reflection coefficient and absorption coefficient spectra of different NCCPA/CF systems as a function of frequency. Within the entire frequency band, the peaks of the absorption coefficient correspond to the valleys of the reflection coefficient, indicating that the synergistic effect between impedance matching and loss mechanisms of the composite has reached the optimal state. Among them, due to effective energy dissipation cycle formed by the NCCPA electromagnetic wave absorption layer and the CF reflection layer, especially for $NCC_{1\text{-}1}PA/CF$, it exhibits a stable and high electromagnetic wave absorption performance.

Combining the structural morphology and EMI shielding performance, Fig. 5(j) illustrates the shielding mechanism of NCCPA/CF with a two-layer coupling structure, which can be summarized as a three-stage synergistic electromagnetic wave loss mechanism of “absorption–reflection–reabsorption”. This is achieved through the special functions and microstructure design of the two-layer unit components, effectively capturing and dissipating electromagnetic energy [53]. When incident electromagnetic wave reaches the sample surface, the appropriate filler ratio and the low-density structure of the PI aerogel optimize the equivalent impedance, making NCCPA match the impedance of free space, thereby reducing surface reflection and allowing more electromagnetic waves to enter the material and complete the initial absorption in the NCCPA layer. In terms of dielectric loss, the continuous conductive network constructed by CNT drives electron migration to generate Joule heat, resulting in conductive loss; The interfaces polarization loss between Ni@C, CNT/Ni@C and the PI matrix; And the dipole polarization loss caused by defects within the Ni@C composite [54]. In terms of magnetic loss, Ni@C composite undergos magnetic moment rearrangement and magnetic domain rotation under the influence of an external magnetic field; simultaneously, the frequency of magnetic moment movement matches the frequency of electromagnetic waves, triggering natural resonance. Besides dielectric loss and magnetic loss, the 3D porous network of PI aerogel leads to multiple scattering and refraction of electromagnetic waves, thus prolonging its propagation loss path. In addition, the high aspect ratio of dielectric CNT and the magnetic response of Ni@C jointly construct a “dielectric-magnetic synergistic network”. In which, magnetic loss broadens the low-frequency absorption window, while dielectric loss enhances high-frequency attenuation, avoiding the contradiction of “strong reflection-low absorption” of electromagnetic waves, thus enabling efficient capture of electromagnetic energy over a wide frequency band. The electromagnetic waves that have not been absorbed through the NCCPA layer reach the bottom CF layer, and the 3D continuous conductive network of CF reflects most of the electromagnetic waves back to the upper NCCPA absorption layer due to its high conductivity. Meanwhile, the double-layer interface between CF and the NCCPA would trigger multiple reflections and interface polarization loss, thereby achieving the multi-mechanism collaborative attenuation of the double-layer structure. In short, the functional partition between the upper “dielectric-magnetic absorption layer” and the lower “conductive reflection layer” enables electromagnetic waves to complete a closed-loop process of “absorption–reflection–reabsorption”. This solves the problems of incomplete absorption in the single absorption layer, as well as the secondary pollution caused by strong reflection caused by single reflection layers, balances low reflectivity and high absorption efficiency, and constructs an electromagnetic wave “capture-dissipation” integrated trap [55].

3.4 Potential integrated applications of NCCPA/CF

Based on the compressive stress–strain curves, cyclic compression durability, and deformation recovery rate of the upper NCCPI aerogel (Fig. S4 in the ESM), the NCCPA/CF two-layer coupling structure can adjust the connectivity of the internal conductive channels through a certain compressive stress. In addition, the continuous rigid network of the lower CF forms a deformation-limited domain effect, which synergistically achieves a bilinear and highly sensitive response of the current change rate ($\Delta I/I_0$) to the compressive stresses. Specifically, as shown in Fig. 6(a), the

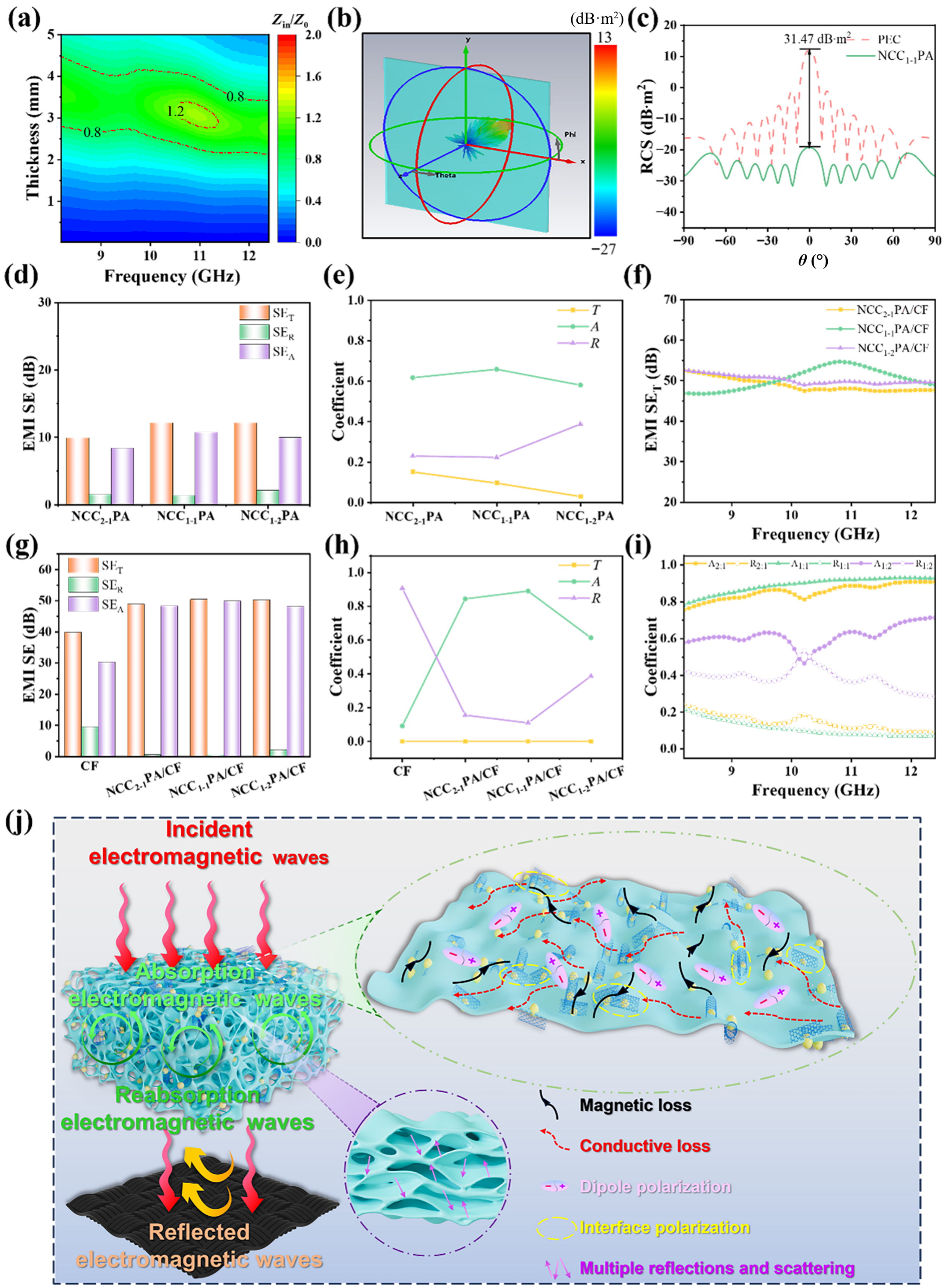

Figure 5 (a) 2D color mapping of $|Z_{in}/Z_0|$ and (b) 3D RCS plots of NCCPA. (c) Simulated RCS curves of the PEC plane as well as PEC planes covered with NCCPA at different angles of incidence. (d) Electromagnetic interference shielding effectiveness (EMI SE) of NCCPA. (e) Transmission (*T*), absorption (*A*), and reflection (*R*) coefficients of NCCPA. (f) Frequency characteristics of EMI SE of NCCPA/CF. (g) EMI SE of CF and NCCPA/CF. (h) *T*, *A*, and *R* coefficients of NCCPA/CF. (i) Frequency characteristics of *A* and *R* of NCCPA/CF. (j) Schematic diagram of EMI shielding mechanism of NCCPA/CF.

sensitivity is 0.011 kPa^{-1} in the low stress region and 0.006 kPa^{-1} in the high stress region, with a goodness of fit $R^2 > 0.99$. During the strain/pressure cyclic loading, the elastic deformation of the sample is mediated by the elastic recovery of the PI matrix and the self-supporting effect of the rigid CNT network, thereby ensuring the anti-fatigue property. The "compression-recovery" reversible characteristic of the pore channels enables highly repeatable responses to different strains and stresses (Figs. 6(b) and 6(c)), while the pore reconstruction dominated deformation mechanism makes the material rate-insensitive to the tensile rate of 1–20 mm/min (Fig. 6(d)), which embodies the structural control logic of the force-electrical response dynamics [56, 57]. It is worth noting that the excellent compression-recovery performance ensures that NCCPA/CF still maintains a good EMI effect after 50 compression cycles (Fig. S5 in the ESM).

Based on the intrinsic localized surface plasmon resonance (LSPR) effect of Ni@C and CNT [58], NCCPA has potential for photothermal conversion. As shown in Fig. 6(e), the maximum sunlight absorption rate of NCCPA is as high as 95%. When NCCPA is coupled with CF fabric, the sunlight absorption rate of the resulting NCCPA/CF composite fiber membrane in the entire UV–Vis–NIR wavelength range is further increased to over 97%. The above results are attributed to the excellent light-harvesting capability of NCCPA, which promotes more incident sunlight to enter the material interior, and the porous microstructure of the aerogel effectively extends the scattering path of sunlight. Additionally, a small amount of sunlight passing through NCCPA is reabsorbed by the CF fabric, further increasing the absorption and utilization efficiency of sunlight (Fig. 6(f)). Specifically, as shown in Figs. 6(g)–6(i), under simulated irradiation conditions of 0.5, 1.0, 1.5, and 2.0 times the sunlight intensity, the surface temperature of NCCPA/CF composite fiber membranes with

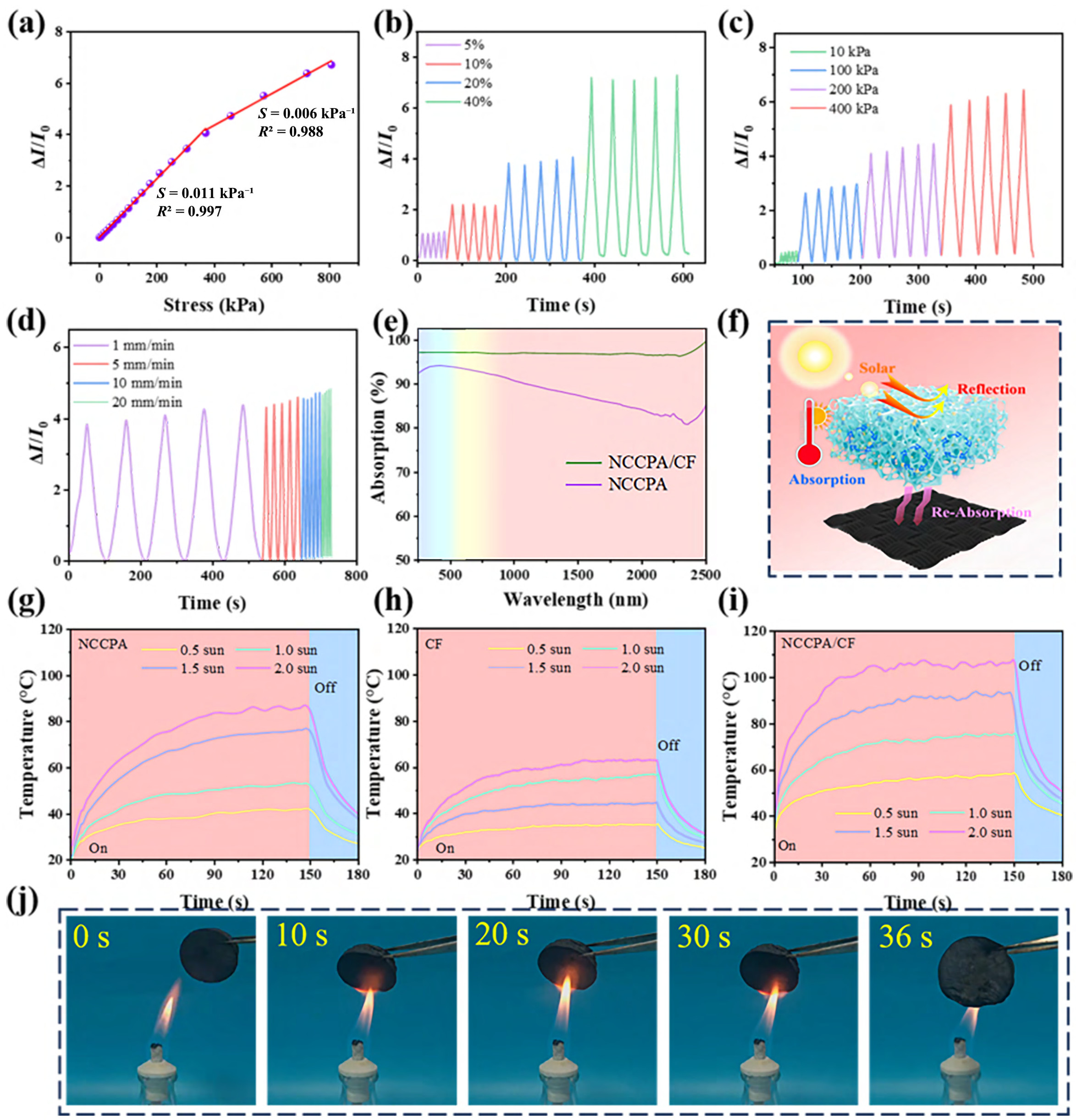

Figure 6 (a) Bilinear response characteristics of piezoresistive sensing, (b) strain cycle fatigue resistance, (c) pressure cycle stability validation, (d) tensile rate insensitivity, (e) broad-spectrum light absorption, (f) photothermal conversion synergistic mechanism, (g) upper photothermal warming kinetics, (h) lower thermal management efficacy, (i) photothermal steady-state temperature distribution, and (j) thermal safety response to direct flame test.

coupled structures rapidly increased to 58.6, 75.5, 93.8, and 107.5 ℃, significantly higher than that of NCCPA and pure CF fabric.

Good flame retardancy is an important foundation for the application of materials in extreme high-temperature thermal environments [59]. Microscale combustion calorimetry (MCC) was employed to systematically characterize the combustion heat release behavior of NCCPA (Fig. S6 in the ESM). The results show that as the processing temperature increases, the peak value of heat release rate (HRR) is only ~ 54 W/g, and it decreases rapidly after reaching the maximum value. This indicates that NCCPA releases heat slowly and mildly during thermal decomposition without violent combustion, and possesses favorable high-temperature self-extinguishing property, demonstrating excellent inherent flame retardancy [60]. For NCCPA/CF, the upper PI aerogel itself has high-temperature thermal stability. The 3D porous network not only inhibits the heat conduction of air in the pores, but also effectively blocks the propagation of flame. Additionally, in high-temperature environments, the Ni@C microspheres catalytically drive the condensation and carbonization process of PI to form a dense high-temperature-resistant carbon layer barrier, blocking the entry of oxygen and thereby inhibiting the combustion reaction. Furthermore, the high thermal conductivity of the lower CF can quickly dissipate heat and avoid thermal runaway caused by heat accumulation. Therefore, under the synergistic effect of the above action mechanisms, even when the NCCPA/CF is placed on the high-temperature flame of an alcohol lamp, there is no combustion generated (Fig. 6(j)).

4 Conclusion

In summary, Ni@C/CNT/PIA//CF(NCCPA/CF) achieves the "absorption–reflection–reabsorption" shielding mechanism for electromagnetic waves through the two-layer coupling effect of the absorption layer Ni@C/CNT/PIA and the reflection layer CF. Specifically, in the Ni@C/CNT/PIA layer, by adjusting the ratio of the dielectric filler CNT to the magnetic filler Ni@C, excellent electromagnetic wave impedance matching performance is achieved in the X-band. When the mass ratio of CNT to Ni@C microspheres is 1:1, the best electromagnetic wave absorption loss performance is achieved, and this result has been further verified through RCS simulation. The high conductivity of CF ensures the effective reflection of electromagnetic waves passed through Ni@C/CNT/PIA to achieve the purpose of reabsorption. In addition, due to its biological sensing detection, photo-thermal conversion and flame-retardant properties, NCCPA/CF may play a role in wearable electronic detection and protection devices, as well as in military and aerospace industries with extreme special requirements.

Electronic Supplementary Material: Supplementary material (preparation methods, analysis of the eddy current loss and attenuation constant formulas, supplementary figures (Figs. S1–S6), and supporting table (Table S1)) is available in the online version of this article at https://doi.org/10.26599/NR.2026.94908888.

Data availability

All data needed to support the conclusions in the paper are presented in the manuscript and the Electronic Supplementary Material. Additional data related to this paper may be requested from the corresponding author upon request.

Acknowledgements

We acknowledge financial support from the Key Research Projects of Higher Education Institutions in Henan Province (No. 25A430007), the Natural Science Foundation of Henan Province (No. 252300420410), the Scientific and Technological Project in Henan Province (No. 262102230001), the Postdoctoral Fellowship Program (Grade B) of China Postdoctoral Science Foundation (No. GZB20240675), the National Natural Science Foundation of China (No. 52503413), and the Excellent Youth Found of Natural Science Foundation of Henan Province (No. 262300421098). The authors also acknowledge the financial support from Princess Nourah bint Abdulrahman University Researchers Supporting Project number (No. PNURSP2026R47), Princess Nourah bint Abdulrahman University, Riyadh, Saudi Arabia.

Declaration of competing interest

All the contributing authors report no conflict of interests in this work.

Author contribution statement

S. M. Z. and S. Q. L. fabricated the samples, performed the measurements, and wrote the manuscript. T. S. A., H. L., W. H. C., N. A., R. B. W., and H. A. participated in discussions and provided valuable suggestions. D. P., C. T. L., Z. H. G., and C. Y. S. supervised the project. All the authors have approved the final manuscript.

Use of AI statement

None.

References

[1] Wang, Q. Q.; Liu, D.; Zhou, J.; Liu, G.; Wang, L. Y.; Wu, R. B. Intelligentization of electromagnetic functional materials: From design to applications. *Adv. Mater.*, in press, DOI: 10.1002/adma.202510212.

[2] Yan, J. T.; Lin, C. X.; Jiang, S.; Wang, W. J.; Zhong, M.; Tang, H.; Guo, R. H. Fabrication of flexible Co_3Fe_7@$Ti_3C_2T_x$/TiO_2/C@Spacer fabrics for tunable radar-infrared compatible stealth Inspired by layered structure of rock. *Chem. Eng. J.* **2024**, *499*, 156409.

[3] Zhang, J. W.; Xu, T. Q.; Ding, L.; Ji, J. P.; Geng, J. X.; Ngo, H. T.; Zhou, K.; Chen, X. K.; Geng, F. X. Bridging graphene for films with superior mechanical and electrical performance for electromagnetic interference shielding. *eScience* **2025**, *5*, 100407.

[4] Wang, L.; Lang, L.; Ren, W. N.; Yang, Z. L.; Gao, T. T.; Zhao, Z. G.; Kallel, M.; Liu, Y. Z. Electrically insulating composite films with excellent electromagnetic interference shielding performance enabled by multilayer structure. *Eng. Sci.* **2025**, *34*, 1477.

[5] Shahzad, F.; Alhabeb, M.; Hatter, C. B.; Anasori, B.; Hong, S. M.; Koo, C. M.; Gogotsi, Y. Electromagnetic interference shielding with 2D transition metal carbides (MXenes). *Science* **2016**, *353*, 1137–1140.

[6] Zhang, Y. L.; Ruan, K. P.; Zhou, K.; Gu, J. W. Controlled distributed $Ti_3C_2T_x$ hollow microspheres on thermally conductive polyimide composite films for excellent electromagnetic interference shielding. *Adv. Mater.* **2023**, *35*, 2211642.

[7] Li, Y. F.; Ding, B. H.; Ma, X. Y.; Bi, Y. J.; Jin, Z. M.; Sun, Y.; Guo, J. H.; Wang, Y. X.; Teng, C. Ethanol-induced stable dispersion and compatibility of MXene in WEP leading to highly ordered layered materials for high electromagnetic interference shielding performance. *Chem. Eng. J.* **2026**, *531*, 172688.

[8] Chen, Y. X.; Zhang, D.; Wu, S. T.; Yang, Y. F.; Meng, W. X.; Lin, Z. Y.; Zhang, Y.; Guo, F. M.; Zhang, Y. J.; Shang, Y. Y. et al. Carbon material films for flexible and efficient electromagnetic interference shielding: A review. *Rare Met.* **2026**, *45*, e70035.
[9] Zhang, Y. L.; Gu, J. W. Ultrathin and flexible electromagnetic interference shielding films by interface-confinement strategy. *Sci. China Mater.* **2026**, *69*, 2968–2969.
[10] Qiao, S. J.; Shi, Z. C.; Tong, A. X.; Huang, Z. Y.; He, A. N.; Wang, B. H.; He, J.; Wang, J. X.; Chen, M.; Huang, Z. X. et al. Inorganic high-performance fiber-based materials for electromagnetic interference shielding: Fundamentals, fabrications, and emerging applications. *Nano-Micro Lett.* **2026**, *18*, 229.
[11] Ding, B. H.; Wang, Y. X.; Li, Y. F.; Jiang, H. T.; Gao, P. Y.; Sun, Y.; Guo, J. H.; Teng, C. Lightweight, rigid, ordered RSF/PVA/MXene aerogels with Janus structure for effective electromagnetic interference shielding with low reflectivity. *Nano Res.* **2026**, *19*, 94908069.
[12] Tan, R.; Bai, W. H.; Yan, J. T.; Geng, L.; Jiang, S. X.; Guo, R. H. Flexible CoNiZn@Ti_3CNT_x MXene@carbon fabrics with hierarchical structure for efficient electromagnetic wave absorption. *Chem. Eng. J.* **2024**, *500*, 157444.
[13] Wei, Y. W.; Bhuyan, P.; Kwon, S. J.; Kim, S.; Bae, Y.; Singh, M.; Thanh Tran, D.; Ha, M.; Jeong, K. U.; Ma, X. et al. Liquid metal grid patterned thin film devices toward absorption-dominant and strain-tunable electromagnetic interference shielding. *Nano-Micro Lett.* **2024**, *16*, 248.
[14] Yan, J. T.; Bai, W. H.; Cui, C.; Jiang, S.; Wang, W. J.; Tang, H.; Guo, R. H. Metal-organic framework-derived lilac flower-like CoNiZnO@nitrogen-doped carbon composites via a trapping microwave strategy for efficient absorption. *J. Mater. Chem. A* **2024**, *12*, 28794–28804.
[15] Zhai, M. Z.; Zhao, S. J.; Guo, H.; Li, X. C.; Shi, X. T.; He, M. K.; Zhang, Y. L.; Gu, J. W. Bionic-structured electromagnetic interference shielding composites. *Sci. Bull.* **2025**, *70*, 2347–2364.
[16] Meng, Y. T.; Cai, B.; Zhou, Y. T.; Zhou, L.; Zhang, Y.; Wang, J. H.; Sarula, G.; Yan, L. T.; Lu, M.; Liang, B. L. et al. Bionic coral reef inspired enhanced scattering of trimetallic LDH self assembled $Ti_3C_2T_x$ MXene for advanced microwave absorption. *Nano Res.* **2025**, *18*, 94907842.
[17] Lang, L.; Ren, W. N.; Men, J. Y.; Mao, X. Y.; Yang, Z. L.; Zhang, S. R.; Wang, L. Advances in electromagnetic interference shielding materials with low reflection. *Eng. Sci.* **2025**, *36*, 1640.
[18] Ming, W.; Yang, L.; Chen, H. X.; Fei, F.; Zhang, H.; Sarula, G.; Wang, J. H.; Wang, T. Y.; Jin, C. Z.; Liang, B. L. et al. High toughness MXene/ANF-CZIF67/ANF "magnetic-electric" Janus film for multifunctional low reflection electromagnetic interference shielding. *Nano Res.* **2025**, *18*, 94907621.
[19] Xiang, L. L.; Pan, D.; Lei, J. T.; AlMasoud, N.; Alomar, T. S.; Issaulu, I. G.; Wang, Y. M.; El-Bahy, Z. M.; Liu, C. T.; Guo, Z. H. et al. Sodium alginate aerogel derived SiC@Co–C 3D network enhances electromagnetic wave absorption and thermal conductivity of PDMS based composite. *Int. J. Biol. Macromol.* **2025**, *306*, 141539.
[20] Wang, S. J.; Zhang, X.; Hao, S. Y.; Qiao, J.; Wang, Z.; Wu, L. L.; Liu, J. R.; Wang, F. L. Nitrogen-doped magnetic-dielectric-carbon aerogel for high-efficiency electromagnetic wave absorption. *Nano-Micro Lett.* **2024**, *16*, 16.
[21] Xu, S.; Jia, Z. R.; Lan, D.; Shi, M. J.; Gao, Z. G.; Wu, G. L. Synergistic polarization relaxation in multi-level hybridization and preferred orientation strategies for electromagnetic wave absorption. *Adv. Funct. Mater.*, in press, DOI: 10.1002/adfm.75567.
[22] Liu, X.; Si, Z. K.; Qian, Y. X.; Wu, L. H.; Xu, X. F.; Wan, G. P.; Wang, G. Z. Gradient-nested organic/inorganic aerogels achieve high mechanical strength and feedback-tunable microwave absorption. *Research* **2026**, *9*, 1074.
[23] Ren, J. N.; Dong, W. H.; Zhong, Y. M.; Idrisheva, Z.; Toshtay, K.; Xie, P. T.; Hou, H. Two dimensional graphene and one dimensional magnetite@polyaniline reinforced epoxy nanocomposites with excellent electromagnetic wave absorption performance prepared by hot pressing method. *Eng. Sci.* **2026**, *39*, 1939.
[24] Mai, T.; Chen, L.; Liu, Q.; Guo, Z. H.; Ma, M. G. Zeolitic imidazolate frameworks derived magnetic nanocage/MXene/nanocellulose bilayer aerogels for low reflection electromagnetic interference shielding and light-to-heat conversion. *Adv. Funct. Mater.* **2025**, *35*, 2417947.
[25] Luo, J. W.; Wang, Y.; Qu, Z. J.; Wang, W.; Yu, D. Anisotropic, multifunctional and lightweight CNTs@$CoFe_2O_4$/polyimide aerogels for high efficient electromagnetic wave absorption and thermal insulation. *Chem. Eng. J.* **2022**, *442*, 136388.
[26] Wang, Z. X.; Gao, Z. G.; Jia, Z. R.; Lan, D.; Wu, G. L. Multi-topological engineering induced synergistic magnetoelectric loss of MXene aerogels for microwave absorption. *Carbon* **2026**, *255*, 121535.
[27] Li, Y. L.; Liu, J. C.; Li, D. S.; Fu, M. M.; Xie, A. M.; Li, W. J.; Liang, H.; Li, Y. G.; Chen, X.; Yu, C. PDMS-encapsulated liquid metal-MXene aerogels for resilient electromagnetic wave absorption in harsh environments. *Rare Met.* **2025**, *44*, 3299–3312.
[28] Xu, W. B.; Yang, Y. R.; Wang, Y. Z.; Zhang, Y. L.; Li, T. H.; Liu, A.; Gong, W.; Gu, J. W. Polymer-based composite fibers for electromagnetic interference shielding. *SusMat* **2026**, *6*, e70071.
[29] Luo, G. Y.; Song, M.; Zhang, Q.; An, L. L.; Shen, T.; Wang, S.; Hu, H. Y.; Huang, X.; Wang, D. L. Advances of synergistic electrocatalysis between single atoms and nanoparticles/clusters. *Nano-Micro Lett.* **2024**, *16*, 241.
[30] Bakytkarim, Y.; Tursynbolat, S.; Mukatayeva, Z. S.; Tileuberdi, Y.; Shadin, N. A.; Assirbayeva, Z. M.; Wang, L. S.; Zhussupova, L. A.; Toktarbay, Z. High-sensitivity electrochemical detection of chlorogenic acid based on Pt@r-GO@MWCNTs ternary nanocomposites modified electrodes. *Eng. Sci.* **2024**, *30*, 1178.
[31] Dong, C. S.; Chen, L.; Lin, W. Q.; Li, Z. P.; Wei, L. J.; Peng, C. H.; Liu, H.; Qi, R. H.; Lu, L.; Zhang, L. Z. Nature-inspired 3D hierarchical carbon nanotube matrices enable extraordinary solar steam generation. *Carbon Energy* **2025**, *7*, e655.
[32] Lei, J.; Li, S.; Shen, Y. F.; Wang, X. Y.; Yang, X.; Wu, H. L.; Guo, H. L.; Liu, H. H.; Zhang, D.; Wang, S. A. Ultrafast synthesis of MOF-derived magnetic Ni@C catalyst for efficient photo-enhanced uranium recovery in real nuclear wastewater. *ACS Nano* **2025**, *19*, 31818–31828.
[33] Tian, L.; Tang, Z. J.; Hao, L. Y.; Dai, T.; Zou, J. P.; Liu, Z. Q. Efficient homolytic cleavage of H_2O_2 on hydroxyl-enriched spinel $CuFe_2O_4$ with dual Lewis acid sites. *Angew. Chem., Int. Ed.* **2024**, *63*, e202401434.
[34] Zhu, L. K.; Jing, B. Q.; Kou, X. Y.; Yuan, P. M.; Li, Y. F.; Li, L. C.; Xu, B. B.; Seok, I.; Hu, D. W. Heteroepitaxial barium titanate/niobium potassium oxide polyimide nanocomposite films for high temperature energy storage. *Eng. Sci.* **2025**, *36*, 1666.
[35] Shao, S. P.; Xing, S. Z.; Bi, K.; Zhao, T. T.; Wang, H.; Tang, Y. X.; Liu, J. R.; Wang, F. L. Fabrication of graphene/polyimide/Co–N–C aerogel with reinforced electromagnetic losses and broadband absorption for highly efficient microwave absorption and thermal insulation. *Chem. Eng. J.* **2024**, *494*, 152976.
[36] Shi, Y. X.; Liang, B. Q.; Gao, H.; Zhao, R.; Dong, Q.; Li, T. X.; Ma, Y.; Gao, W.; Zhang, J.; Gu, J. W. et al. Research progress on spherical carbon-based electromagnetic wave absorbing composites. *Carbon* **2024**, *227*, 119244.
[37] Cai, Y. F.; Wang, Z. H.; Fei, G. X.; Lavorgna, M.; Xia, H. S. Polyimide derived carbon/graphene hybrid aerogel microspheres for strong and wide bandwidth microwave absorption. *Adv. Funct. Mater.* **2025**, *35*, 2419252.
[38] Liu, A.; Xu, X. S.; Qiu, H.; Guo, H.; He, M. K.; Yu, Z.; Zhang, Y. L.; Gu, J. W. Bioinspired hollow heterostructure fillers for enhanced electromagnetic interference shielding in polyimide aerogels. *InfoMat* **2025**, *7*, e70060.
[39] Yin, Q.; Li, X.; Qin, Y. T.; Fan, K.; Wang, X.; Liu, X. Y. Fabrication of ultralarge curvature folding-resistant polyimide films by widening

the elastic range and intermolecular slippery spacing. *Macromolecules* **2023**, *56*, 4362–4370.

[40] Yang, F. L.; Zhao, X.; Usman, K. A. S.; Jiang, D. G.; Razal, J. M.; Wang, J. H.; Tao, J. L.; Zhang, J. Z. Engineering coaxial MXene@CNT fibers via wet-spinning for balanced mechanical, electrical, and electrochemical performance. *J. Energy Storage* **2025**, *137*, 118719.

[41] Akamatsu, K.; Fujii, M.; Tsuruoka, T.; Nakano, S. I.; Murashima, T.; Nawafune, H. Mechanistic study on microstructural tuning of metal nanoparticle/polymer composite thin layers: Hydrogenation and decomposition of polyimide matrices catalyzed by embedded nickel nanoparticles. *J. Phys. Chem. C* **2012**, *116*, 17947–17954.

[42] Wang, J. E.; Ming, W.; Chen, L. F.; Song, T. L.; Yele, M.; Zhang, H.; Yang, L.; Sarula, G.; Liang, B. L.; Yan, L. T. et al. MoS_2 lubricate-toughened MXene/ANF composites for multifunctional electromagnetic interference shielding. *Nano-Micro Lett.* **2025**, *17*, 36.

[43] Qi, W. W.; Xiang, L.; Ning, M. Q.; Liu, T.; Li, Y. Y.; Zhuang, X. H.; Lv, G. G.; Wu, Q.; Tan, G. G.; Jiang, Q. Z. et al. Dual-oxides confined carbonyl iron enabling superior electromagnetic wave absorption and anticorrosion performance. *Nano Mater. Sci.* **2026**, *8*, 446–456.

[44] Zhang, X.; Xin, G. M.; Wu, N.; Pan, F.; Liu, J. R.; Zeng, Z. H. Recent advances in metal-organic frameworks for electromagnetic wave absorption. *Research* **2025**, *8*, 0876.

[45] Hu, Y. P.; Zhou, T.; Zhang, D. H.; Lei, Z.; Liu, D. J.; Qin, S. H.; Zou, K. X. Constructing ternary core–shell structured MWCNTs@Co/C@PANI nanocomposite for microwave absorption. *Rare Met.* **2025**, *44*, 10594–10606.

[46] Wang, L. L.; Zhao, X. F.; Yu, Y.; Hua, X. F.; Wei, R. B. Enriching carbon nanotubes in poly (arylene ether nitrile) porous films for enhanced electromagnetic shielding properties. *Eng. Sci.* **2025**, *38*, 1912.

[47] Wang, X.; Chen, X. M.; He, Q. Y.; Hui, Y. Z.; Xu, C. F.; Wang, B. C.; Shan, F. H.; Zhang, J.; Shao, J. Y. Bidirectional, multilayer MXene/polyimide aerogels for ultra-broadband microwave absorption. *Adv. Mater.* **2024**, *36*, 2401733.

[48] Khotthada, S.; Matthujak, A.; Khamphakdi, P.; Glinubon, J.; Siriboon, C.; Salangam, I.; Phongthanapanich, S. Development and performance analysis of an electromagnetic needle-free jet injection device for efficient drug delivery in pig farms. *Eng. Sci.* **2025**, *33*, 1329.

[49] Qi, C. Z.; Min, P.; Zhou, X. F.; Jin, M.; Sun, X.; Wu, J. J.; Liu, Y. J.; Zhang, H. B.; Yu, Z. Z. Multifunctional asymmetric bilayer aerogels for highly efficient electromagnetic interference shielding with ultrahigh electromagnetic wave absorption. *Nano-Micro Lett.* **2025**, *17*, 291.

[50] Duan, C. Q.; Guan, L.; Han, S. J.; Zhu, Y. J.; Huang, Z. Y.; Cheng, K. Q.; Zhang, Y. Y.; Yuan, X. L.; Zhao, B.; Zhang, R. Exceptional electromagnetic wave absorption in high-entropy carbides enabled by lattice distortion engineering. *Rare Met.* **2026**, *45*, e70171.

[51] Gu, W. H.; Sheng, J. Q.; Huang, Q. Q.; Wang, G. H.; Chen, J. B.; Ji, G. B. Environmentally friendly and multifunctional shaddock peel-based carbon aerogel for thermal-insulation and microwave absorption. *Nano-Micro Lett.* **2021**, *13*, 102.

[52] Tan, R. Y.; Liu, Y. J.; Li, W. J.; Zhou, J. T.; Chen, P.; Zavabeti, A.; Zeng, H. B.; Yao, Z. J. Multi-scale dispersion engineering on biomass-derived materials for ultra-wideband and wide-angle microwave absorption. *Small Methods* **2024**, *8*, 2301772.

[53] Li, M. M.; Zhang, M. L.; Zhao, Y. J.; Jiang, S.; Xu, Q. Y.; Han, F. Y.; Zhu, J. H.; Liu, L. F.; Ge, A. X. Multilayer structured CNF/rGO aerogels and rGO film composites for efficient electromagnetic interference shielding. *Carbohydr. Polym.* **2022**, *286*, 119306.

[54] Cui, P. Y.; Zou, P. B.; Kang, Y. F.; Yan, X.; Zhou, X.; Wang, B. K.; Wu, F.; Pan, S. B.; Ma, J. C.; Huang, W. H. Large-scale facile synthesis of biomass fibers and high-entropy metal hierarchical porous carbon toward enhanced electromagnetic absorption. *Research* **2025**, *8*, 0868.

[55] Zhang, S.; Liang, C. M.; Zhou, L.; Wu, J. T.; Koo, M. C.; Wu, Z. X.; Chen, Y. T.; Wang, G. S. Heterolayered carbonized MXene/polyimide aerogel for low-reflection electromagnetic interference shielding and multi-spectrum compatible protection. *Nano-Micro Lett.* **2026**, *18*, 204.

[56] Zhang, D. W.; Butt, H.; Zheng, L. X. Emerging trends of ionic sensors for electronic skin (e-Skin). *ES Mater. Manuf.* **2025**, *30*, 1849.

[57] Gao, S. Y.; Guo, H.; Guo, Y. Q.; Qiu, H.; Gong, W.; Gu, J. W. Superior through-plane thermal conductivity in carbon fibers/spherical graphene/epoxy laminated composites for low-altitude aircrafts. *InfoMat* **2026**, *8*, e70139.

[58] Gao, Y.; Chen, X.; Jin, X.; Zhang, C. J.; Zhang, X.; Liu, X. D.; Li, Y. H.; Li, Y.; Lin, J. J.; Gao, H. Y. et al. Multifunction integration within magnetic CNT-bridged MXene/CoNi based phase change materials. *eScience* **2024**, *4*, 100292.

[59] Zhang, D. Q.; Liu, J. J.; Williams, B. L.; Hou, Z. L.; Lofink, B. J.; Santos, V. H.; Becher, E. M.; Shrestha, S. B.; Nasir, Z.; Patel, H. et al. Enhancing flame retardancy of polyurethane foam with montmorillonite-based nanocoatings. *ES Mater. Manuf.* **2024**, *26*, 1228.

[60] Jiang, H.; Xie, Y. H.; He, M. K.; Li, J. D.; Wu, F.; Guo, H.; Guo, Y. Q.; Xie, D. L.; Mei, Y.; Gu, J. W. Highly thermally conductive and flame-retardant waterborne polyurethane composites with 3D BNNS bridging structures via magnetic field assistance. *Nano-Micro Lett.* **2025**, *17*, 138.